ADVANCED ELECTRONIC MATERIALS
www.advelectronicmat.de

Frank–van der Merwe Growth versus Volmer–Weber Growth in Successive Stacking of a Few-Layer Bi_2Te_3/Sb_2Te_3 by van der Waals Heteroepitaxy: The Critical Roles of Finite Lattice-Mismatch with Seed Substrates

*Hoseok Heo, Ji Ho Sung, Ji-Hoon Ahn, Fereshte Ghahari, Takashi Taniguchi, Kenji Watanabe, Philip Kim, and Moon-Ho Jo**

Integration of dissimilar 2D materials held together by van der Waals (vdw) interactions enables exploration of new electronic and optical phenomena in 2D solid-state, because coherent stacking of dissimilar 2D units can form another new class of 2D electronic systems.[1–9] Recent research on stacked heterostructures of diverse 2D vdw-layered materials, such as graphene, hexagonal boron nitride (*h*-BN), transition-metal dichalcogenides, and other layered chalcogenides, has called attention to the large-area integration of such 2D units by conventional gas-phase deposition.[10–15] Typically, vdw heteroepitaxy is characterized by the presence of heterointerfaces formed on a surface free of chemical polarity or dangling bonds, so the coherent epitaxial growth is not strictly affected by strain built up by the in-plane lattice-mismatch at the interfaces between the two dissimilar crystal planes.[16,17] This means that the vdw growth habits are not strongly dependent on the choice of the growth substrates in various gas-phase growth methods.[18–23] However, the effects of the finite lattice-mismatch during the sequential 2D stacking growth of layered chalcogenides have not been systematically addressed to date.[24–27] Here, by employing sequential stacking growth of Bi_2Te_3 and Sb_2Te_3, we demonstrate two distinct vdw growth modes, which are determined by the strain of the growth substrates, i.e., layer-by-layer growth (Volmer–Weber type) on *h*-BN substrates and 3D-island growth (Frank–van der Merwe type) on SiO_2/Si substrates.

Bi_2Te_3 and Sb_2Te_3 form a rhombohedral (space group R3m) crystal symmetry consisting of hexagonally close-packed atomic layers. The unit layer in a sequence of Te–Bi(Sb)–Te–Bi(Sb)–Te, termed as a quintuple layer (QL), is repeated along the *c*-axis with the lattice constants, a = 4.383 Å and c = 30.487 Å for Bi_2Te_3, and a = 4.250 Å and b = 30.350 Å for Sb_2Te_3.[28] These unit layers are bound weakly to each other by the vdw coupling, but the atoms within the layers are covalently bonded to form 2D hexagonal lattices. In our study, a few-QL Bi_2Te_3 and Sb_2Te_3 crystals were grown by chemical vapor deposition using powder precursors. The heteroepitaxial Bi_2Te_3-Sb_2Te_3 stacking growth was accomplished by sequential growth of Bi_2Te_3 as the first step and Sb_2Te_3 as the second step for 5 min at each step. 200 mg of high-purity Bi_2Te_3 or Sb_2Te_3 (99.99%) powders were placed in alumina boats, then loaded in a hot-walled quartz-tube furnace (1.5″ diameter and 12″ long). As the growth substrates we used either mechanically exfoliated *h*-BN[29] transferred onto SiO_2/Si substrates, or SiO_2 (300 nm)/Si. The substrates were placed 10 cm downstream from the tube center at the appropriate location in the temperature gradient along the tube furnace. Prior to heating, the furnace was evacuated to 10^{-3} Torr and purged with 100 sccm of high-purity N_2 for 30 min to eliminate residual oxygen. Then the center of furnace were heated to 540 °C for Bi_2Te_3 growth, within 30 min by flowing 5 sccm of high-purity Ar flow as a carrier gas at a total pressure of 0.1 Torr. Then, the Sb_2Te_3 growth as the second growth step in another tube furnace, where it was heated to 530 °C with Ar 5 sccm and total pressure of 0.1 Torr for 5 min.

The sequential two-step stacking growth resulted in significantly different morphologies of a few-QL Bi_2Te_3/Sb_2Te_3 stacks, depending on whether the substrate was *h*-BN or SiO_2/Si. **Figure 1**a,b shows the case of Bi_2Te_3/Sb_2Te_3 stacking on SiO_2/Si substrates, where the bottom Bi_2Te_3 layers grow as triangular facet crystals, and the top Sb_2Te_3 layers initially nucleate at the Bi_2Te_3 crystal edge and grow onward on the first layers as triangular facets. The top Sb_2Te_3 crystals are relatively thick with the typical thickness ranged 0–40 nm (9–37 QLs), as shown in

H. Heo, J. H. Sung, Dr. J.-H. Ahn,[+] Prof. M.-H. Jo
Center for Artificial Low Dimensional Electronic Systems
Institute for Basic Science (IBS)
37673, South Korea
E-mail: mhjo@postech.ac.kr

H. Heo, J. H. Sung
Division of Advanced Materials Science
Pohang University of Science and Technology (POSTECH)
Pohang 37673, South Korea

Dr. F. Ghahari, Prof. P. Kim
Department of Physics
Harvard University
Cambridge, MA 02138, USA

Dr. T. Taniguchi, Dr. K. Watanabe
Advanced Materials Laboratory
National Institute for Materials Science
1-1 Namiki, Tsukuba 305-0044, Japan

Prof. M.-H. Jo
Department of Materials Science and Engineering and
Division of Advanced Materials Science
Pohang University of Science and Technology (POSTECH)
Pohang 37673, South Korea

[+]Present address: Department of Electronic Material Engineering, Korea Maritime and Ocean University, 727 Taejong-ro, Yeongdo-gu, Busan 49112, South Korea

DOI: 10.1002/aelm.201600375

 © 2017 WILEY-VCH Verlag GmbH & Co. KGaA, Weinheim

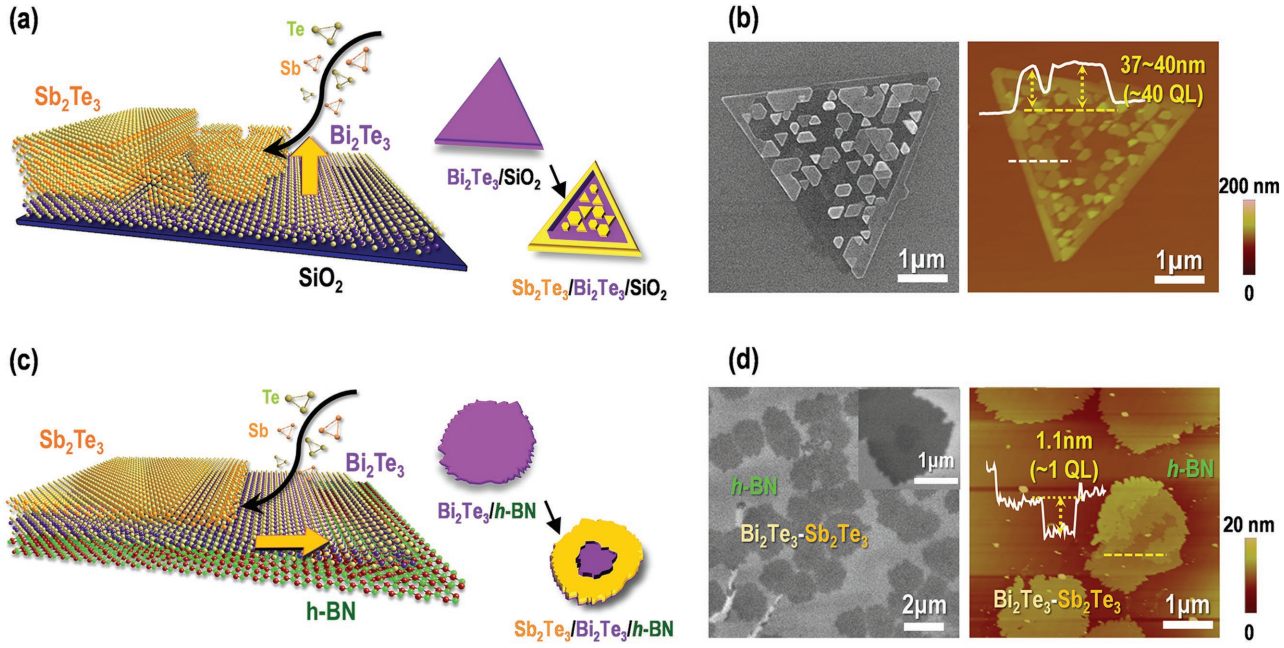

Figure 1. a) Schematics of sequential two-step stacking growth of the few-QL Sb_2Te_3/Bi_2Te_3 stacks on SiO_2/Si substrates. b) A representative optical microscope image and an atomic force microscope (AFM) image of Sb_2Te_3/Bi_2Te_3 stacks on SiO_2/Si substrate. Inset in the AFM image is the height profile along the white dotted line. c) Schematics of sequential two-step stacking growth of the few-QL Sb_2Te_3/Bi_2Te_3 stacks on *h*-BN substrates. d) A representative optical microscope image and an AFM image of Sb_2Te_3/Bi_2Te_3 stacks on *h*-BN substrates. The height profile in the AFM image show the top Sb_2Te_3 layer is 1 QL in thickness.

the atomic force microscope (AFM) image in Figure 1b. On the contrary, on *h*-BN substrates (Figure 1c,d), neither the first Bi_2Te_3 nor the second Sb_2Te_3 crystals formed characteristic triangular facets—see also Figure S1 in the Supporting Information. More importantly, each layer was typically atomically thin. The second Sb_2Te_3 layers of 1 QL nucleate at the edge of the first layer and the growth propagate layer-by-layer (**Figure 2**d).

First, we discuss on the first Bi_2Te_3 layer growth in which the crystal morphology was different on *h*-BN than on SiO_2/Si. On SiO_2/Si substrates, a few-QL thick Bi_2Te_3 were crystallized as triangular or hexagonal facets spanning over a few tens of micrometers in lateral size with 8–10 QLs in thickness (Figure 2a,b).[30] By contrast, on *h*-BN substrates, Bi_2Te_3 crystals were irregularly shaped without noticeable facets of denser population with smaller lateral size (a few micrometers) and thinner thickness (<4 QLs) (Figure 2c,d). This difference in crystal shapes implies that underlying substrates critically influence the vapor phase growth mode. The substrate-dependent growth characteristics of various low-dimensional nanocrystals in both solution and vapor phase growth have been discussed for their growth mechanisms.[31,32] In general, within the framework of the nucleation kinetics model, a gas-phase growth reaction can be divided into two steps: (1) adsorption of vaporized precursors onto substrates and diffusion to the preferential growth sites and (2) incorporation of precursors into existing nuclei. The rate-limiting step in our vapor phase crystal growth can be determined as either the diffusion-limited step or the reaction-limited step . On *h*-BN substrates, adatom diffusion ($D_{s,h\text{-BN}}$) into the nuclei edge can be sufficiently faster than adatom diffusion (D_{s,Bi_2Te_3}) on the pre-existing crystals. Consequently, at the growth front, adatoms randomly incorporate onto nucleus edges, and therefore form irregular crystal shapes instead of thermodynamically stable facets. This assumption is qualitatively valid considering the lower surface energy of *h*-BN, $\gamma_{h\text{-BN}} \approx 65$–$75$ mJ m^{-2}, which lacks dangling bonds, than that of SiO_2, $\gamma_{SiO_2} \approx 300$–$400$ mJ m^{-2},[33–35] as similarly discussed elsewhere.[36] On SiO_2/Si substrates adatom diffusion (D_{s,SiO_2}) is relatively slow, due to surface roughness and dangling bonds of amorphous SiO_2 (i.e., $D_{s,h\text{-BN}} > D_{s,Bi_2Te_3} > D_{s,SiO_2}$), and crystal growth is limited by the incorporation reaction rate into nucleus. As a result, crystallization occurs at thermodynamically stable lattice sites, producing distinct facets at the growth front. In our 2D crystal growth, the rate-limiting step can be further verified by observing the crystal shape evolution as a function of several growth parameters. For example, if growth is reaction-limited, facet growth is favorable at high vapor pressure, and the crystal shape tends to become increasingly faceted as vapor pressure increases.[37] In our study, we observed such morphology variation by varying vapor pressure (Figure S2, Supporting Information), and thus we infer that the Bi_2Te_3 crystal growth on *h*-BN occurs in the reaction-limited regime. Instead, on SiO_2/Si substrates, the 2D Bi_2Te_3 crystals always crystallized to characteristic facets, regardless of the vapor pressure; i.e., crystal growth is diffusion-limited.

We now discuss the second layer growth mode as the main theme of this work. The detailed heteroepitaxial relationship of Bi_2Te_3/Sb_2Te_3 stacks on *h*-BN was confirmed further by cross-sectional transmission electron microscopy (TEM) investigations (**Figure 3** and Figure S3, Supporting Information). The TEM specimens were fabricated using a conventional focused ion beam technique. The few-QL Bi_2Te_3/Sb_2Te_3 stacks were easily damaged during the ion milling, presumably due to

© 2017 WILEY-VCH Verlag GmbH & Co. KGaA, Weinheim

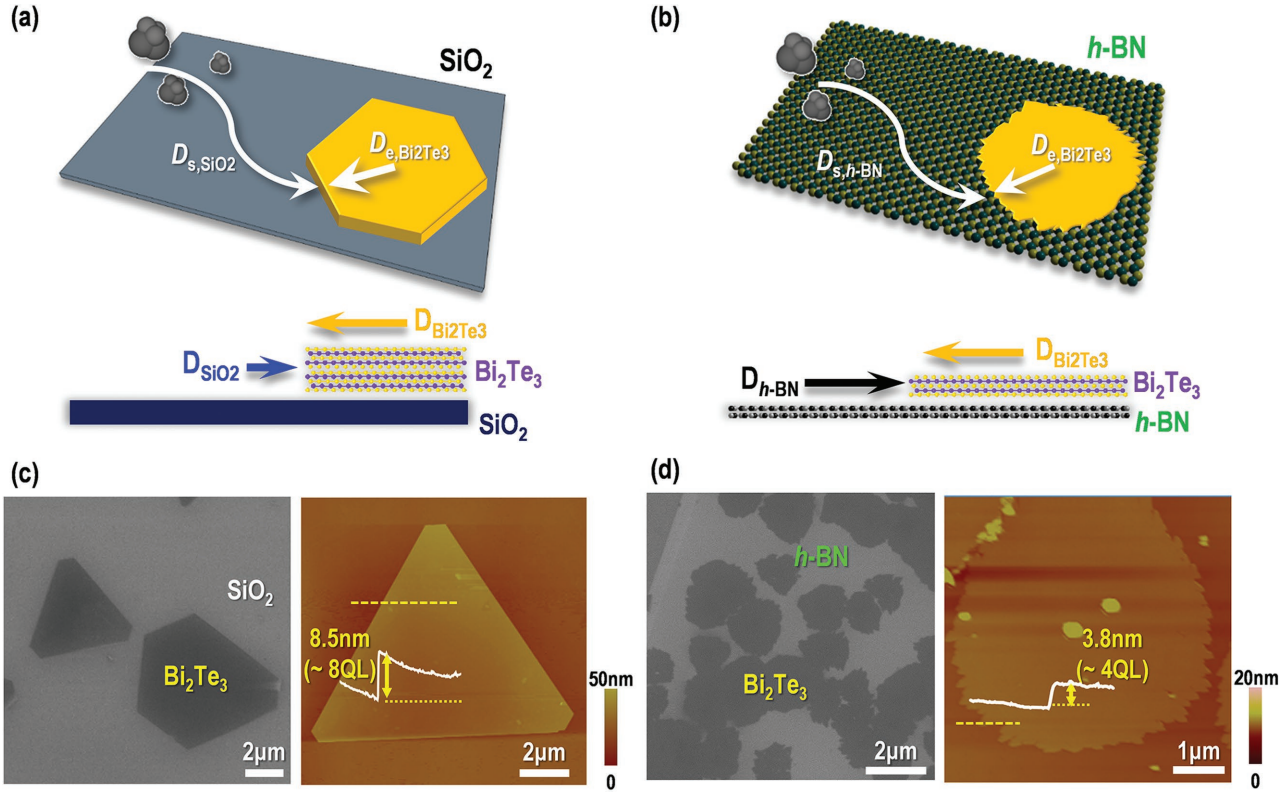

Figure 2. a,b) Growth schematics of the first few-QL Bi_2Te_3 crystals on a) SiO_2/Si substrates and b) *h*-BN substrates. Representative optical microscope image and an AFM images of the few-QL Bi_2Te_3 on c) SiO_2/Si and d) *h*-BN substrates.

thermal damage. Therefore we intentionally prepared thicker Bi_2Te_3/Sb_2Te_3 stacks of 10-QL thickness. Low-magnification TEM images were taken of the stacks on *h*-BN (Figure 3a), and high-magnification images were taken at Bi_2Te_3/*h*-BN and Bi_2Te_3/Sb_2Te_3 interfaces from which fast Fourier transformation (FFT) patterns were extracted (Figure 3b,c). The few-QL Bi_2Te_3 grew epitaxially on *h*-BN with in-plane orientation relation of *h*-BN(10-10)/Bi_2Te_3(01–10) and out-of-plane relation of *h*-BN(0002)/Bi_2Te_3(00015). We also examined the heteroepitaxial relation between Bi_2Te_3 and Sb_2Te_3 stacks by using annular dark-field scanning TEM (ADF-STEM). The atomic contrast in images and intensity profiles along the *c*-axis (Figure 3d) indicate that individual QLs of Bi_2Te_3 and Sb_2Te_3 were composed of the alternating layer sequence of Te–Bi–Te–Bi–Te and Te–Sb–Te–Sb–Te, respectively. Note that the intensity variation is weaker in Sb_2Te_3 due to small atomic number difference. Considering all these experimental observations, we can develop a schematic diagram of the heteroepitaxial orientation relation (Figure 3e). From Figure 3b, we extracted the (01–10) inter-planar spacing ($d_{(01-10)}$) of Bi_2Te_3 layers on *h*-BN, which corresponds to an *a*-axis lattice constant of 4.34–4.35 Å and, thus the in-plane lattice-mismatch was ≈0.76%–0.96%. Additionally, we found that the *a*-axis lattice constant of Bi_2Te_3 layers is thickness-dependent and can be as large as ≈4.2% in the thinnest Bi_2Te_3 of 2 QLs (Figure S4, Supporting Information). We have also obtained Raman scattering spectra on Bi_2Te_3 layers, in which one can expect red or blue shifts of Raman peaks, depending on the fact that the strain is tensile or compressive[24,38] (Figure S5, Supporting Information). We find a blue-shift (≈2.4 cm^{-1}) of the in-plane (E^2_g) vibration mode, while a red-shift (≈1.3 cm^{-1}) of the out-of-plane (A^2_{1g}) vibration mode in Bi_2Te_3 (6 QLs) on *h*-BN, comparing with those of Bi_2Te_3 crystals (5 QLs) on SiO_2. In the meanwhile, $a_{Bi_2Te_3}$ on SiO_2/Si substrates was estimated to be 4.377–4.393 Å, which is almost identical to the bulk values.[28] This difference between the in-plane lattice parameters of the first Bi_2Te_3 layers on the two substrates also verifies that the first Bi_2Te_3 layers on *h*-BN are under significant compressive strain, but were relaxed on amorphous SiO_2 substrates. We assume that the bottom Te atoms in Bi_2Te_3 minimize the inter-atomic columbic interaction energy by stacking on hollow sites in the *h*-BN lattices, instead of stacking directly on top B or N atoms; this stacking on hollow sites also occurs the InAs/graphene vdw epitaxy system.[39] We also confirm the heteroepitaxial relationship of Bi_2Te_3/Sb_2Te_3 stacks on SiO_2/Si substrate by in-plane TEM analysis (Figure S6, Supporting Information).

As discussed earlier in Figure 1, the second layer (Sb_2Te_3) growth mode on the first layer of Bi_2Te_3 is markedly different when the underlying substrate is *h*-BN or SiO_2. On Bi_2Te_3/*h*-BN, growth occurs layer-by-layer (Frank–van der Merwe mode), but on Bi_2Te_3/SiO_2 it occurs by 3D island formation (Volmer–Weber mode). Thus, the residual strain in the first Bi_2Te_3 layers has a significant influence on the second Sb_2Te_3 growth.[40–46] To determine the specific growth modes, we considered the degree of adatom surface diffusion during vapor phase growth of Sb_2Te_3 on Bi_2Te_3/*h*-BN and Bi_2Te_3/SiO_2. Adatom surface

© 2017 WILEY-VCH Verlag GmbH & Co. KGaA, Weinheim

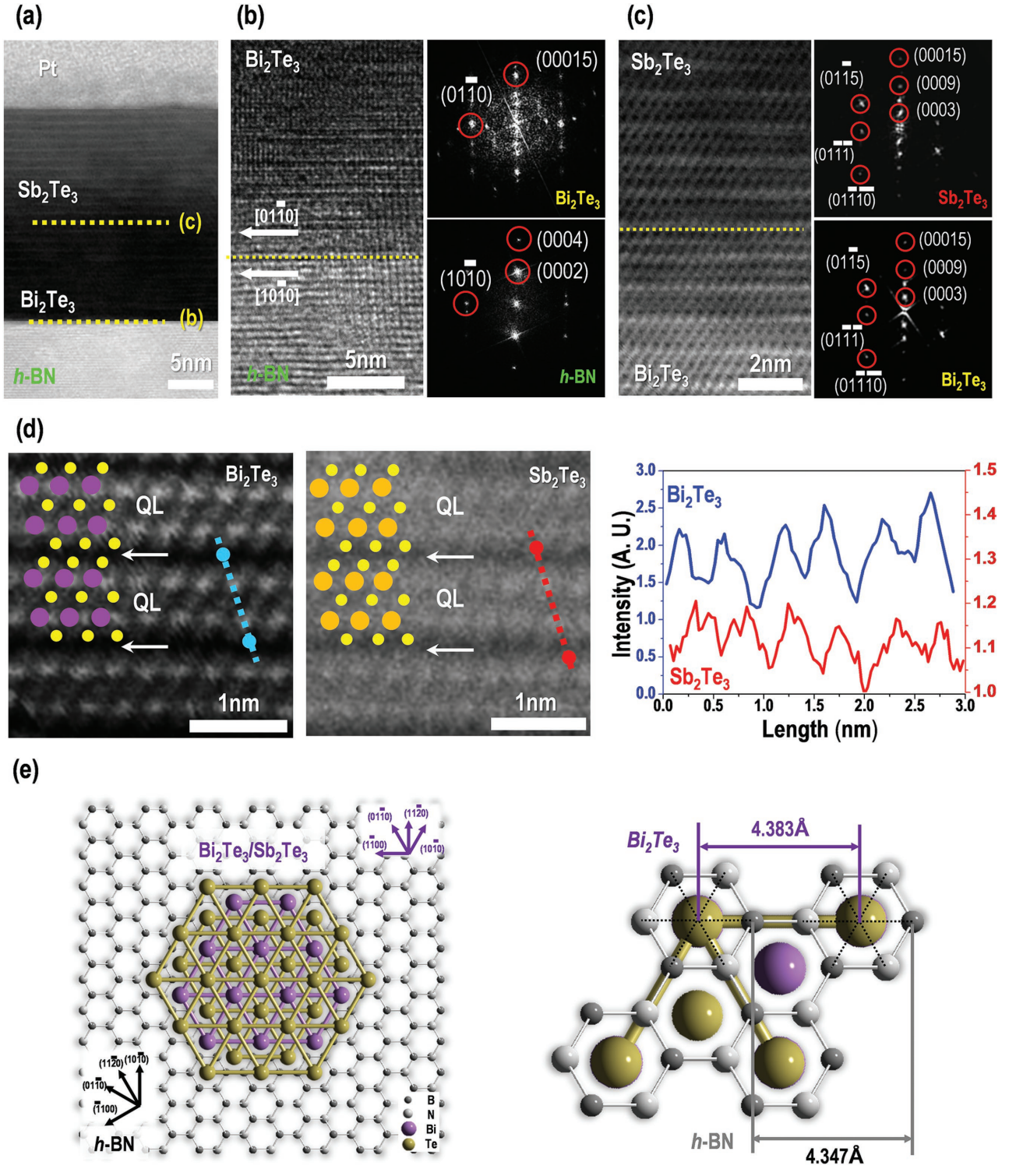

Figure 3. a) Low magnification cross-sectional transmission electron microscope (TEM) image of Sb_2Te_3/Bi_2Te_3 stacks on *h*-BN substrates. The *h*-BN/Bi_2Te_3 and Bi_2Te_3/Sb_2Te_3 heterointerfaces are marked as yellow dotted lines. b) A high resolution TEM image at the *h*-BN/Bi_2Te_3 interface and the corresponding fast Fourier transformation (FFT) pattern of the *h*-BN and Bi_2Te_3 regions. c) A high angle annular dark-field (HAADF) scanning TEM image at the Bi_2Te_3/Sb_2Te_3 interface and the corresponding FFT patterns of Bi_2Te_3 and Sb_2Te_3 regions. d) (left and middle) High-magnification HAADF-STEM images of Bi_2Te_3 and Sb_2Te_3 layers, and (right) the contrast intensity profiles along the blue (Bi_2Te_3) and red (Sb_2Te_3) dotted lines. e) In-plane atomic configurations developed from the heteroepitaxial stacks of *h*-BN(10–10)//Bi_2Te_3(01–10) in (a–d).

© 2017 WILEY-VCH Verlag GmbH & Co. KGaA, Weinheim

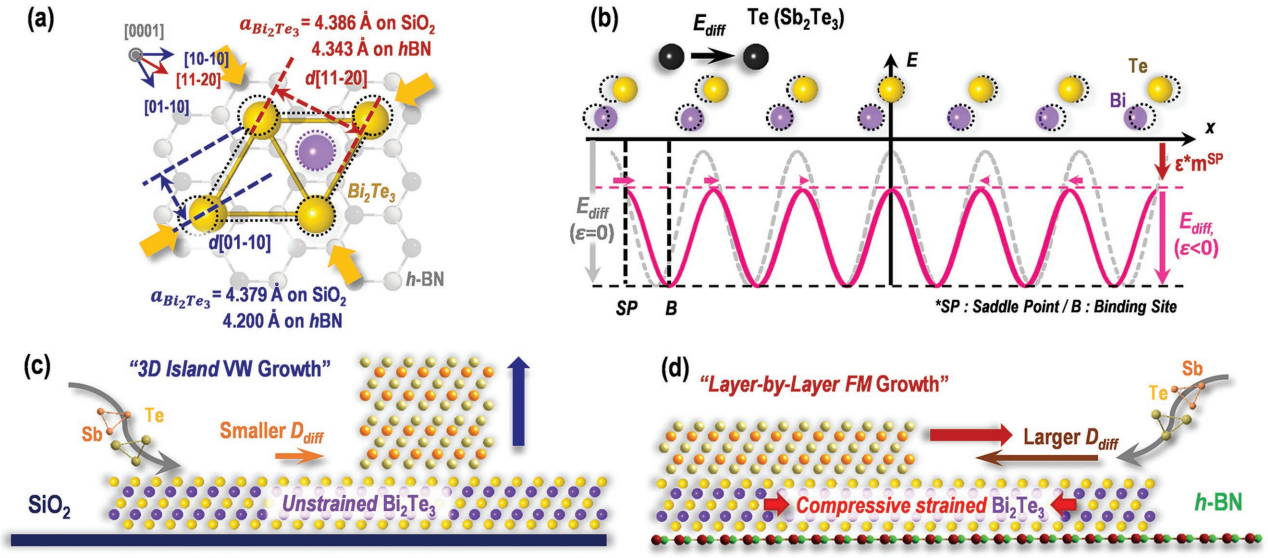

Figure 4. a) In-plane atomic configurations defining in-plane lattice constant of Bi_2Te_3 ($a_{Bi_2Te_3}$) estimated from two different interplanar spacing $d_{Bi_2Te_3(01\text{–}10)}$ and $d_{Bi_2Te_3(11\text{–}20)}$ from FFT patterns of the TEM images. b) Schematics of adatom surface diffusion during the second step Sb_2Te_3 stacking onto Bi_2Te_3 surfaces. The relationship between the diffusion energy barrier (E_{diff}) and strain (ε) shows the change in E_{diff} in the presence of compressive strain on Bi_2Te_3/*h*-BN stacks, compared to unstrained Bi_2Te_3/SiO_2 stacks. Two different growth modes of Sb_2Te_3 on c) unstrained Bi_2Te_3/SiO_2/Si substrates (3D island growth) and d) on compressive strained Bi_2Te_3/*h*-BN substrates (layer-by-layer growth).

diffusion can be described by diffusion barrier energy (E_{diff}) which is the energy required to move an adatom between two adjacent nearest sites on a surface. Then, the diffusion coefficient (D) can be expressed as $D = A\cdot\exp\{-E_{diff}/(kT)\}$, where A, k, and T are the diffusion constant, Boltzmann constant, and temperature. In general, E_{diff} increases under tensile strain and decreases under compressive strain (**Figure 4**b),[40,42–44] where E_{diff} is the energy difference between the saddle point (V^{SP}) and the binding site (V^{B}). In our case, the saddle points are occupied by the topmost Te atoms with the nearest distance and the binding site is a hollow atomic site in the hexagonal lattice. With the presence of strain, the saddle point energy and the binding site energy vary differently in that strain-induced elastic dipole moment, called "force dipole tensor (m)" is much larger at the saddle points than at the binding sites ($m^{SP} > m^{B}$). Consequently, this situation can be expressed as a function of strain as

$$E_{diff}(\varepsilon) = V^{SP} - V^{B} + \varepsilon\left(m^{SP} - m^{B}\right) \quad (1)$$

where V^{SP} and V^{B} are the potential energy at the saddle points and at the binding sites under the unstrained condition, ε corresponds to strain exerted on the lattice, and m^{SP} and m^{B} are force dipole tensors at the saddle points and the binding sites, respectively.[40] On the compressively strained Bi_2Te_3, the equilibrium distance between adjacent Te atoms are compressed out of the original positions as defined in unstrained Bi_2Te_3; as a result E_{diff} decreases (equivalently $D_{Bi_2Te_3}$ increases) for adatom surface diffusion (Figure 4b). Consequently, this enhanced surface diffusion of adatoms facilitates stable edge nucleations for layer-by-layer growth (Figure S7, Supporting Information). Meanwhile during the growth on Bi_2Te_3/SiO_2/Si, the adatom diffusion is slow over the relatively larger E_{diff}, and causes 3D island growth (Figure 4c,d).

The quality of the 2D Bi_2Te_3 crystals grown on *h*-BN (5 QLs) by the layer-by-layer growth were characterized by low temperature electron transport at 2 K. Employing electron-beam lithography, we fabricated multiple electrodes for the magnetoresistance and Hall measurements as in the upper inset of **Figure 5**a. Figure 5a shows the longitudinal (R_{xx}) and Hall (R_{xy}) resistivity in the presence of the perpendicular magnetic field (B) up to 15 T. We estimated the 2D carrier density $n \approx 1.1 \times 10^{13}$ cm^{-2} from the linearly increasing R_{xy} as a function of B (the lower inset of Figure 5). The main panel of Figure 5 shows R_{xx} smoothly changing with B. From these data sets, we estimate the electron mobility $\mu \approx 2500$ m^2 V^{-1} s^{-1}, implying possible observation of the quantum oscillation at high magnetic field ranges. In order to confirm high magnetic quantum oscillation in magnetoresistance, we subtract a smooth parabolic background $R_{xx}^{poly}(B)$ obtained from a polynomial fit (dashed line in Figure 5(a)) from $R_{xx}(B)$. Figure 5(b) display the difference $\Delta R_{xx} = R_{xx} - R_{xx}^{poly}$ versus $1/B$. ΔR_{xx} displays a sequence of oscillating features in uniform separation of Δ $(1/B)$, suggesting the occurrence of Shubnikov–de Haas (SdH) oscillations in our samples at the high magnetic field range. The SdH oscillations, the successive emptying of the Landau levels with increasing magnetic field, can be due to the presence of the topological surface states in our Bi_2Te_3 crystals grown on *h*-BN.[47,48] The reasonably high carrier mobility and the measurable conductivity quantum oscillations at low temperatures, which are comparable to molecular beam epitaxy grown crystals,[49,50] are notable for chemical vapor-phase grown crystals, supporting a high 2D crystal quality with minimum defects.

© 2017 WILEY-VCH Verlag GmbH & Co. KGaA, Weinheim

ADVANCED ELECTRONIC MATERIALS
www.advelectronicmat.de

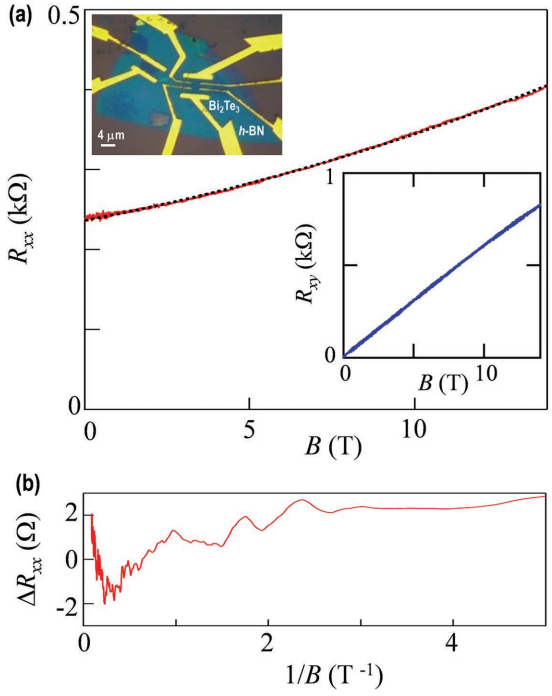

Figure 5. a) The longitudinal resistance R_{xx} of Bi_2Te_3 on *h*-BN substrates in the presence of the perpendicular magnetic field B at 2 K. The black dashed line is the polynomial fit to obtain a smooth background $R_{xx}^{poly}(B)$. (Lower inset) R_{xy} as a function B measured in the same condition for R_{xx}. (Upper inset) an optical microscope image of a Bi_2Te_3/*h*-BN device. b) $R_{xx} - R_{xx}^{poly}$ versus $1/B$ showing a Shubnikov–de Haas oscillation.

Supporting Information

Supporting Information is available from the Wiley Online Library or from the author.

Acknowledgements

This work was supported by Institute for Basic Science (IBS), Korea under the Project Code (IBS-R014-G1-2016-a00). P. K. acknowledges support from AFOSR (FA9550-14-1-0268).

Received: September 13, 2016
Revised: December 18, 2016
Published online: January 20, 2017

[1] A. K. Geim, I. V. Grigorieva, *Nature* **2013**, *499*, 419.
[2] L. Britnell, R. M. Ribeiro, A. Eckmann, R. Jalil, B. D. Belle, A. Mishchenko, Y.-J. Kim, R. V. Gorbachev, T. Georgiou, S. V. Morozov, A. N. Grigorenko, A. K. Geim, C. Casiraghi, A. H. Castro Neto, K. S. Novoselov, *Science* **2013**, *340*, 1311.
[3] L. Britnell, R. V. Gorbachev, R. Jalil, B. D. Belle, F. Schedin, A. Mishchenko, T. Georgiou, M. I. Katsnelson, L. Eaves, S. V. Morozov, N. M. R. Peres, J. Leist, A. K. Geim, K. S. Novoselov, L. A. Ponomarenko, *Science* **2012**, *335*, 947.
[4] M. Bernardi, M. Palummo, J. C. Grossman, *Nano Lett.* **2013**, *13*, 3664.
[5] C. R. Dean, L. Wang, P. Maher, C. Forsythe, F. Ghahari, Y. Gao, J. Katoch, M. Ishigami, P. Moon, M. Koshino, T. Taniguchi, K. Watanabe, K. L. Shepard, J. Hone, P. Kim, *Nature* **2013**, *497*, 598.
[6] C.-H. Lee, G.-H. Lee, A. M. van der Zande, W. Chen, Y. Li, M. Han, X. Cui, G. Arefe, C. Nuckolls, T. F. Heinz, J. Guo, J. Hone, P. Kim, *Nat. Nanotechnol.* **2014**, *9*, 676.
[7] H. Heo, J. H. Sung, S. Cha, B.-G. Jang, J.-Y. Kim, G. Jin, D. Lee, J.-H. Ahn, M.-J. Lee, J. H. Shim, H. Choi, M.-H. Jo, *Nat. Commun.* **2015**, *6*, 8372.
[8] M.-J. Lee, J.-H. Ahn, J.-H. Sung, H. Heo, S. G. Jeon, W. Lee, J. Y. Song, K.-H. Hong, B. Choi, S.-H. Lee, M.-H. Jo, *Nat. Commun.* **2016**, *7*, 12011.
[9] S. Cha, J.-H. Sung, S. Sim, J. Park, H. Heo, M.-H. Jo, H. Choi, *Nat. Commun.* **2016**, *7*, 10768.
[10] Z. Liu, L. Song, S. Zhao, J. Huang, L. Ma, J. Zhang, J. Lou, P. M. Ajayan, *Nano Lett.* **2011**, *11*, 2032.
[11] Y. Gong, J. Lin, X. Wang, G. Shi, S. Lei, Z. Lin, X. Zou, G. Ye, R. Vajtai, B. I. Yakobson, H. Terrones, M. Terrones, B. K. Tay, J. Lou, S. T. Pantelides, Z. Liu, W. Zhou, P. M. Ajayan, *Nat. Mater.* **2014**, *11*, 1135.
[12] X. Zhang, F. Meng, J. R. Christanson, C. Arroyo-Torres, M. A. Lukowski, D. Liang, J. R. Schmidt, S. Jin, *Nano Lett.* **2014**, *14*, 3047.
[13] Y. Shi, W. Zhou, A.-Y. Lu, W. Feng, Y.-H. Lee, A. L. Hsu, S. M. Kim, K. K. Kang, H. Y. Yang, L.-J. Li, J.-C. Idrobo, J. Kong, *Nano Lett.* **2012**, *12*, 2784.
[14] H. Heo, J.-H. Sung, G. Jin, J.-H. Ahn, K. Kim, M.-J. Lee, S. Cha, H. Choi, M.-H. Jo, *Adv. Mater.* **2015**, *27*, 3803.
[15] J.-H. Ahn, M.-J. Lee, H. Heo, J.-H. Sung, K. Kim, H. Hwang, M.-H. Jo, *Nano Lett.* **2015**, *15*, 3703.
[16] A. Koma, *Thin Solid Films* **1992**, *216*, 72.
[17] A. Koma, *Surf. Sci.* **1992**, *267*, 29.
[18] S. Xu, Y. Han, X. Chen, Z. Wu, L. Wang, T. Han, W. Ye, H. Lu, G. Long, Y. Wu, Y. Cai, K. M. Ho, Y. He, N. Wang, *Nano Lett.* **2015**, *15*, 2645.
[19] J.-T. Mlack, A. Rahman, G. L. Johns, K. J. T. Livi, N. Markovic, *Appl. Phys. Lett.* **2013**, *102*, 193108.
[20] Q. Ji, Y. Zhang, T. Gao, Y. Zhang, D. Ma, M. Liu, Y. Chen, X. Qiao, P.-H. Tan, M. Kan, J. Feng, Q. Sun, Z. Liu, *Nano Lett.* **2013**, *13*, 3870.
[21] H. Li, J. Cao, W. Zheng, Y. Chen, D. Wu, W. Dang, K. Wang, H. Peng, Z. Liu, *J. Am. Chem. Soc.* **2012**, *134*, 6132.
[22] H. Peng, W. Dang, J. Cao, Y. Chen, D. Wu, W. Zheng, H. Li, Z.-X. Shen, Z. Liu, *Nat. Chem.* **2012**, *4*, 281.
[23] P. Gehring, B. F. Gao, M. Burghard, K. Kern, *Nano Lett.* **2012**, *12*, 5137.
[24] W. Dang, H. Peng, H. Li, P. Wang, Z. Liu, *Nano Lett.* **2010**, *10*, 2870.
[25] S. Wang, X. Wang, J. H. Warner, *ACS Nano* **2015**, *9*, 5246.
[26] Y. Gong, S. Lei, G. Ye, B. Li, Y. He, K. Keyshar, X. Zhang, Q. Wang, J. Lou, Z. Liu, R. Vajtai, W. Zhou, P. M. Ajayan, *Nano Lett.* **2015**, *15*, 6135.
[27] L. Samad, S. M. Bladow, Q. Ding, J. Zhuo, R. M. Jacobberger, M. S. Arnold, S. Jin, *ACS Nano* **2016**, *10*, 7039.
[28] R. W. G. Wyckoff, *Crystal Structures*, Vol. *2*, Wiley, New York **1964**.
[29] K. Watanabe, T. Taniguchi, H. Kanda, *Nat. Mater.* **2004**, *3*, 404.
[30] D. Kong, W. Dang, J. J. Cha, H. Li, S. Meister, H. Peng, Z. Liu, Y. Cui, *Nano Lett.* **2010**, *10*, 2245.
[31] D. J. Eaglesham, M. Cerullo, *Phys. Rev. Lett.* **1990**, *64*, 1943.
[32] M. Guo, P. Diao, S. Cai, *J. Solid State Chem.* **2005**, *178*, 1864.
[33] J. N. Coleman, M. Lotya, A. O'Neill, S. D. Bergin, P. J. King, U. Khan, K. Young, A. Gaucher, S. De, R. J. Smith, I. V. Shvets, S. K. Arora, G. Stanton, H.-Y. Kim, K. Lee, G. Y. Kim, G. S. Duesberg, T. Hallam, J. J. Boland, J. J. Wang, J. F. Donegan, J. C. Grunlan, G. Moriarty, A. Shmeliov, R. J. Nicholls, J. M. Perkins, E. M. Grieveson,

© 2017 WILEY-VCH Verlag GmbH & Co. KGaA, Weinheim

K. Theuwissen, D. W. McComb, P. D. Nellist, V. Nicolosi, *Science* **2011**, *331*, 568.
[34] J. Mizele, J. L. Dandurand, J. Schott, *Surf. Sci.* **1985**, *162*, 830.
[35] R. Cabriolu, P. Ballone, *Phys. Rev. B* **2010**, *81*, 155432.
[36] L. Huang, Y. Yu, C. Li, L. Cao, et al. *J. Phys. Chem. C.* **2013**, *117*, 6469.
[37] T.-C. Chang, I.-S. Hwang, T. T. Tsong, *Phys. Rev. Lett.* **1999**, *83*, 1191.
[38] Yu. I. Yuzyuk, R. S. Katiyar, V. A. Alyoshin, I. N. Zakharchenko, D. A. Markov, E. V. Sviridov, *Phys. Rev. B.* **2003**, *68*, 104104.
[39] Y. J. Hong, W. H. Lee, Y. Wu, R. S. Ruoff, T. Fukui, *Nano Lett.* **2012**, *12*, 1431.
[40] M. Schroeder, D. E. Wolf, *Surf. Sci.* **1997**, *375*, 129.
[41] H. Brune, *Surf. Sci. Rep.* **1998**, *31*, 121.
[42] H. Röder, K. Bromann, H. Brune, K. Kern, *Surf. Sci.* **1997**, *376*, 13.
[43] C. Ratsch, A. P. Setisonen, M. Scheffler, *Phys. Rev. B.* **1997**, *55*, 6750.
[44] H. Brune, K. Bromann, H. Röder, K. Kern, J. Jacobsen, P. Stoltze, K. Jacobsen, J. No/rskov, *Phys. Rev. B.* **1995**, *52*, R14380.
[45] E. Zoethout, O. Gűrlű, H. J. W. Zandvliet, B. Poelsema, *Surf. Sci.* **2000**, *452*, 247.
[46] S. V. Ghaisas, *Surf. Sci.* **1989**, *223*, 441.
[47] D.-X. Qu, Y. S. Hor, J. Xiong, R. J. Cava, N. P. Ong, *Science* **2010**, *329*, 821.
[48] J. H. Sung, H. Heo, I. Hwang, M. Lim, D. Lee, K. Kang, H. C. Choi, J.-H. Park, S.-H. Jhi, M.-H. Jo, *Nano Lett.* **2014**, *14*, 4030.
[49] K. Hoefer, C. Becker, D. Rata, J. Swanson, P. Thalmeier, L. H. Tjeng, *Proc. Natl. Acad. Sci. USA* **2014**, *111*, 14979.
[50] H.-T. He, G. Wang, T. Zhang, I.-K. Sou, G. K. L. Wong, J.-N. Wang, H.-Z. Lu, S.-Q. Shen, F.-C. Zhang, *Phys. Rev. Lett.* **2011**, *106*, 166805.

 © 2017 WILEY-VCH Verlag GmbH & Co. KGaA, Weinheim